Supplementary Materials

Shape memory of bcc structured High-entropy-alloy nanowires during room temperature deformation

Zhanxin Wang[1], Shuai Li[1], Huibin Lian[1], Yufeng Zhao[1], Zhipeng Li[1], Yadi Zhai[2], Haibo Long[2], Lihua Wang[2], Xiaodong Han[2]

[1]School of Physics and Optoelectronic Engineering, Beijing University of Technology, Beijing 100124, China.
[2]Faculty of Materials and Manufacturing, Beijing University of Technology, Beijing 100124, China.

Correspondence to: Prof. Yadi Zhai, Faculty of Materials and Manufacturing, Beijing University of Technology, No. 100 Pingleyuan, Chaoyang District, Beijing 100124, China. E-mail: ydzhai@bjut.edu.cn; Prof. Haibo Long, Faculty of Materials and Manufacturing, Beijing University of Technology, No. 100 Pingleyuan, Chaoyang District, Beijing 100124, China. E-mail: hblong@bjut.edu.cn; Prof. Lihua Wang, Faculty of Materials and Manufacturing, Beijing University of Technology, No. 100 Pingleyuan, Chaoyang District, Beijing 100124, China. E-mail: wlh@bjut.edu.cn

Modelling method:

The initial random solid solution sample was constructed by randomly populating atomic sites with Hf, Nb, Ta, Ti and Zr atoms, subject to the near-equiatomic elemental composition constraint. In order to introduce short range disordering (SRO), the HEA elemental distribution was optimized by performing Monte Carlo (MC) site-occupancy swaps between pairs of sites at a temperature of 300 K. The acceptance of each MC swap conforms to the Metropolis criterion[1]. The MC steps are interchanged with molecular dynamics (MD) relaxation (under a NPT ensemble) steps to efficiently converge site occupancy and atomic displacements (10 MC swaps were performed each followed by 100 MD relaxation steps). The MD time step was set at 1 fs and 4×10^6 steps (iterations) were performed.

Nudged elastic band (NEB) calculation:

6 initial and final structures were constructed for NEB[2–4] calculations by modulating the element distribution. The NEB calculation in our model was carried out using 48 replicas with the modified NEB method[5]. The calculation program won't stop until the maximum value of the norm of the 3N-dimensional force vector of each replica dropping below 0.001 eV/Å, and then the minimum energy paths of these phase transitions can be obtained, as shown in Figures S21 and S22.

The Warren–Cowley parameter (WCP):

WCP was employed to characterize the SRO in the 1st-nearest neighbor shell[5]:

$$WCP_{ij} = 1 - N_{ij}/(F_j N_i) \quad (1)$$

where N_{ij} is the number of j-type atoms around i-type atoms, N_i is the total number of atoms around i-type atoms, and F_j is the atomic fraction of j-type atoms in the HEA. If $WCP_{ij} = 0$, ij-type pairs are randomly distributed (no SRO). If $WCP_{ij} < 0$, ij pairs are more abundant than random, while if $WCP_{ij} > 0$, ij-type pairs occur less often than random.

The Interval Common Neighbour Analysis (i-CNA) method:

The main process of CNA is to calculate the index (ijk) for the bonds between the central atom and its nearest neighbors. The index i is the number of bonded neighbors shared with the central atom; j is the number of bonds between shared neighbors; k is the number of bonds in the longest chain formed by shared neighbors. For a BCC type atom, there are 8 666-type bonds and 6 888-type bonds; for a HCP type atom, there are 6 421-type bonds and 6 422-type bonds; and for a FCC type atom, there are 12 421-type bonds[6].

To account for the resulting variability in the distance between bonded pairs, a threshold r_c is introduced which defines nearest neighbours as those whose distance satisfies $r < r_c$. I-CNA investigates every meaningful threshold by inserting bonds one at a time, in sorted order (short to long). By enumerating all thresholds choices, the intervals in which the structure is unchanged are mapped out. By performing an exhaustive threshold search, the i-CNA method achieves a better structural recognition rate in local environments with larger atomic perturbations. And a Bain transformation has been introduced as a test for classification bias, which was shown that i-CNA is unbiased[6].

Figures. S1–S22

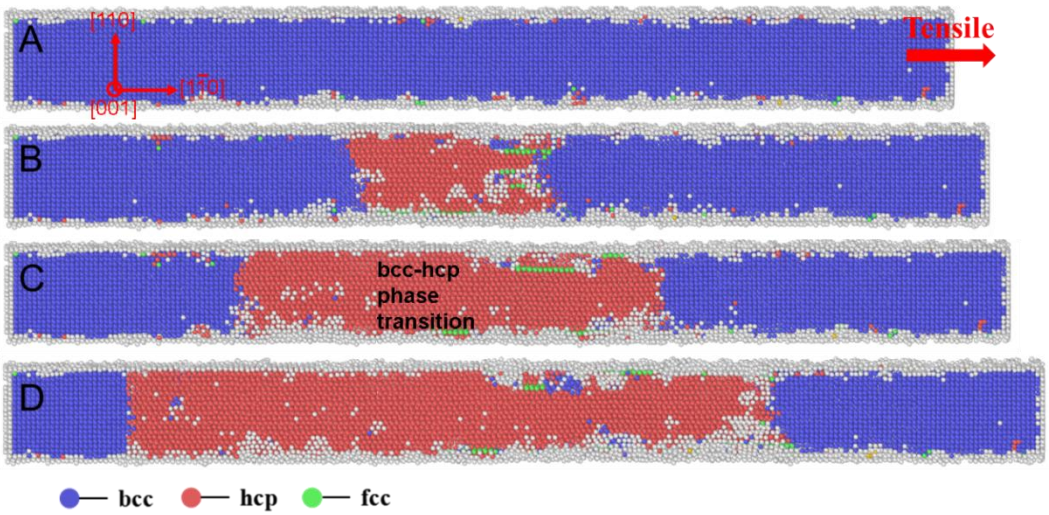

Figure S1. (A-D) illustrates the atomic configuration evolution of the [1$\bar{1}$0]-oriented HfNbTaTiZr HEA NW during stretching at a strain rate of 5×10^{7}. The bcc-hcp phase transition occurs and extends continuously and uniformly.

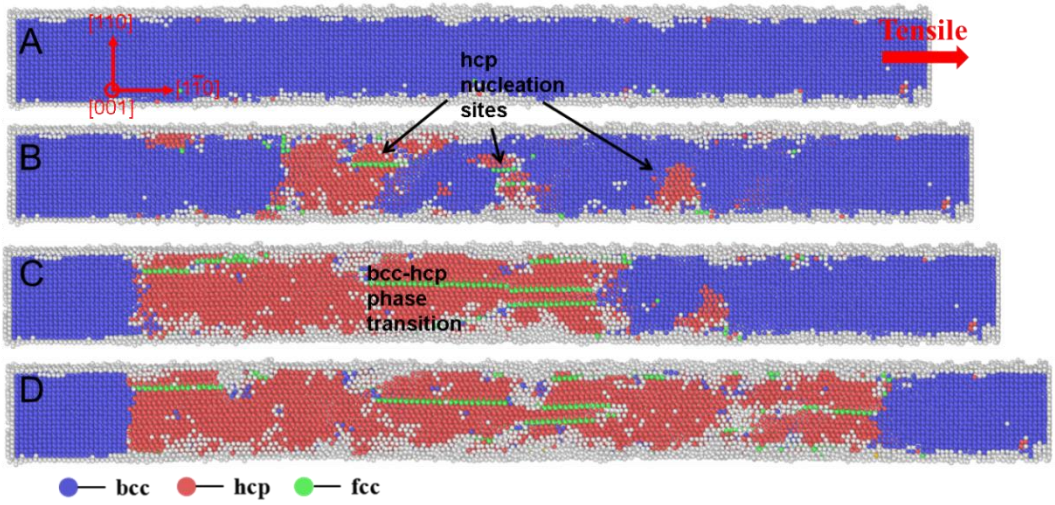

Figure S2. (A-D) illustrates the atomic configuration evolution of the [1$\bar{1}$0]-oriented HfNbTaTiZr HEA NW during stretching at a strain rate of 5×10^{8}. The bcc-hcp phase transition is initiated at multiple sites simultaneously.

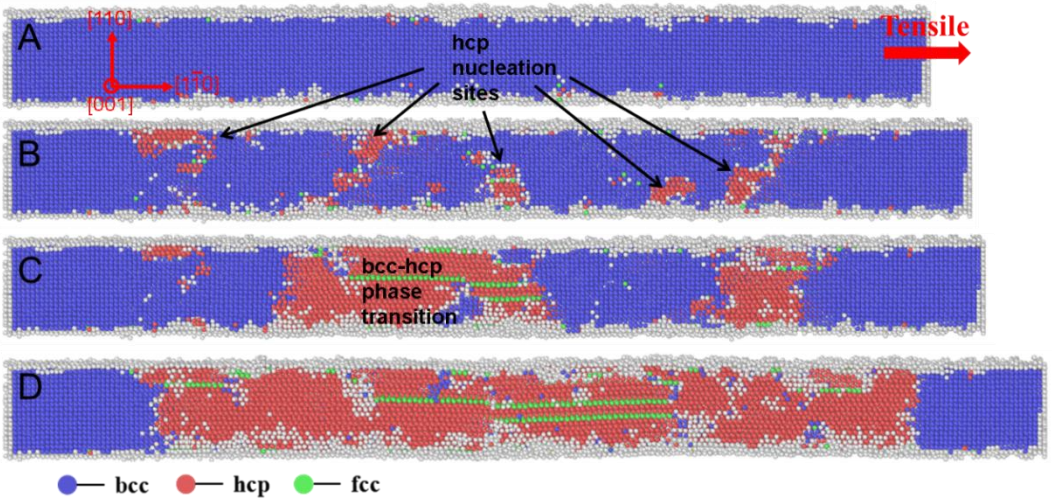

Figure S3. (A-D) illustrates the atomic configuration evolution of the [1$\bar{1}$0]-oriented HfNbTaTiZr HEA NW during stretching at a strain rate of 1×10^{9}. The bcc-hcp phase transition is initiated at more sites simultaneously.

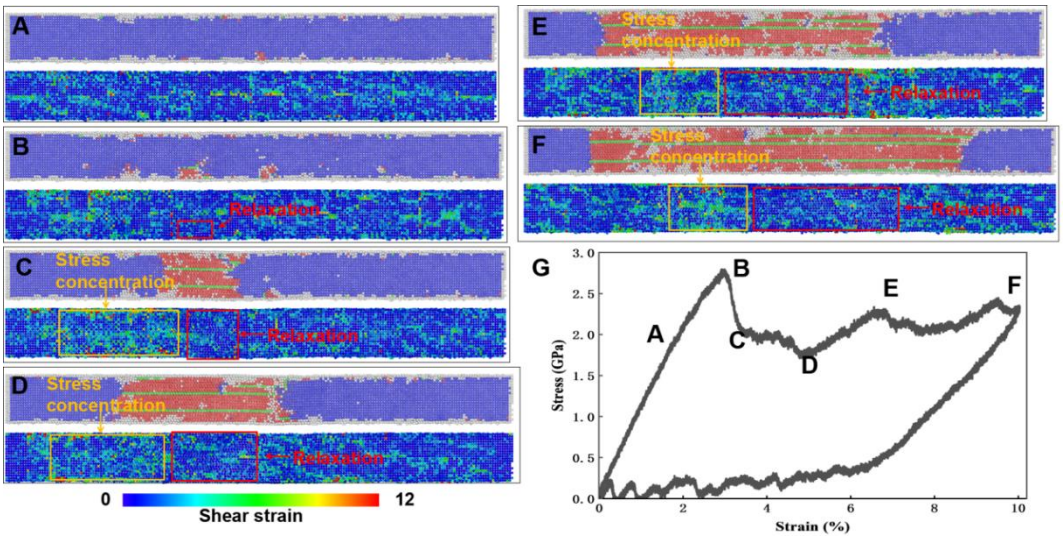

Figure S4. (A-F) Illustrates the shear strain map of the HfNbTaTiZr HEA NW during bcc-hcp phase transition. (G) Presents the stress-strain curve during the tension and compression loading. (A) The strain/stress distribution is relatively uniform when the NW is in elastic stage (the stage before "B" in G). (B-D) As tension continues, the stress will reach a critical value of ~2.7 GPa (the state "B" in G), at which point the bcc-hcp phase transition is initiated, followed by a rapid relaxation of the overall stress (the stage of "B-D" in G). (E,F) As the hcp phase grows to a sufficient size, a portion of the stress/strain is concentrated in the hcp phase. Deformation occurs within the hcp phase region, leading to fluctuations in the stress curve (the stage of "D-F" in G).

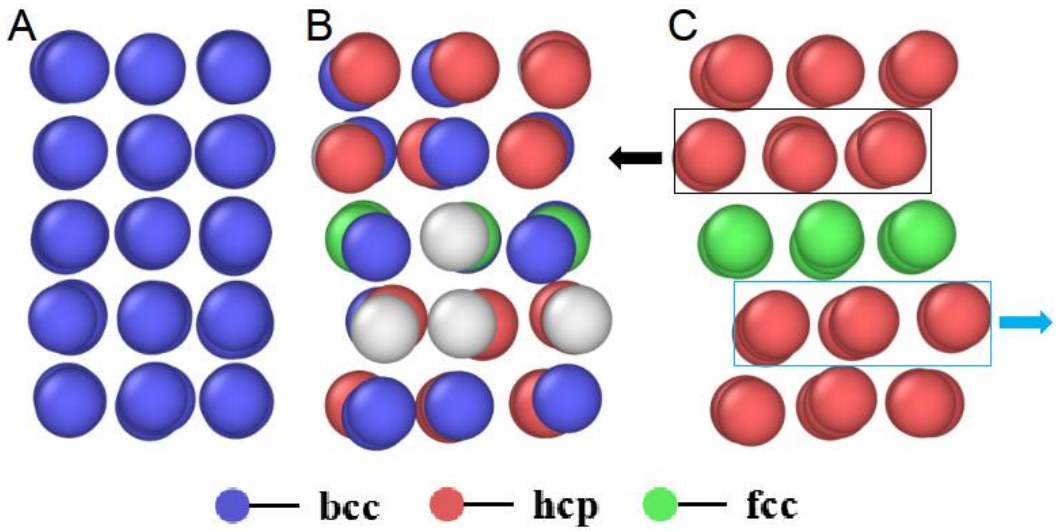

Figure S5. (A-C) illustrates how the fcc atoms are formed via the Bain straining path. (A) The crystal structure of NW is bcc. (B) Lattice is distorted and some other types of crystals are formed. (C) The bcc phase is completely changed into the hcp phase with a layer of fcc atoms in the middle, which is the result from atoms in its upper and lower atomic layers moving to the left and right, respectively.

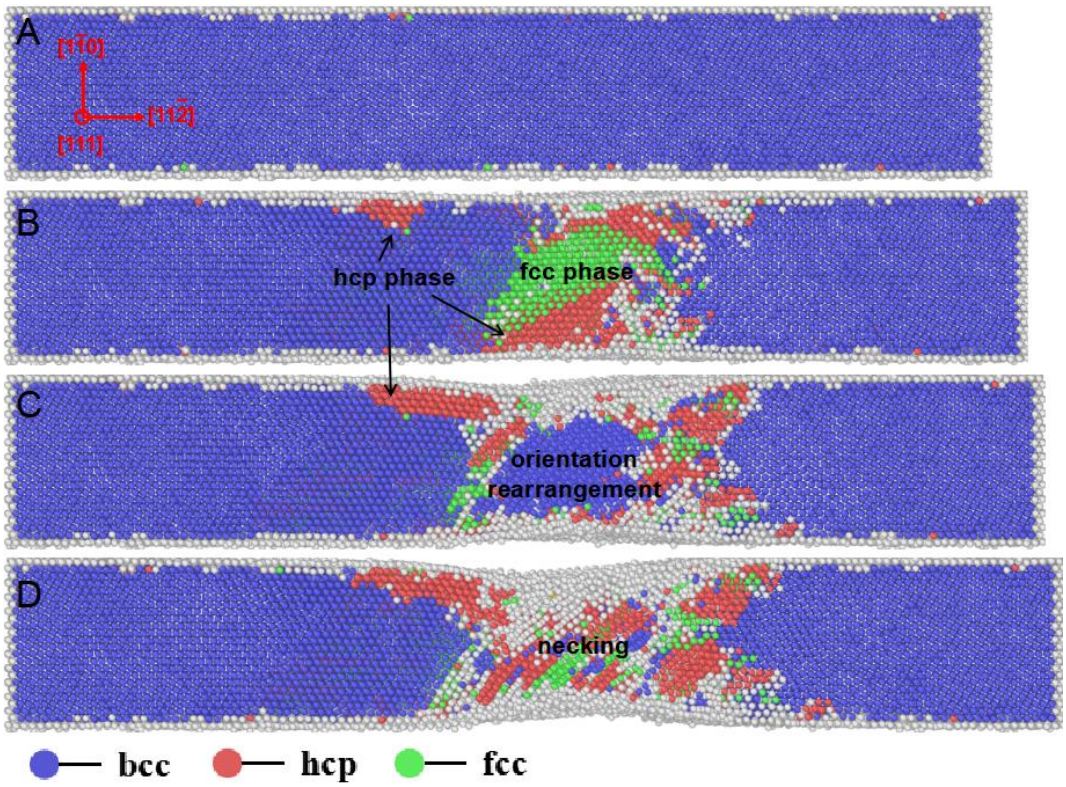

Figure S6. (A-D) illustrates the atomic configuration evolution of a [11$\bar{2}$]-oriented HfNbTaTiZr HEA NW during tension. One can see that the plastic deformation of this NW is mainly controlled by bcc-fcc phase transition, bcc-hcp transition and orientation rearrangement.

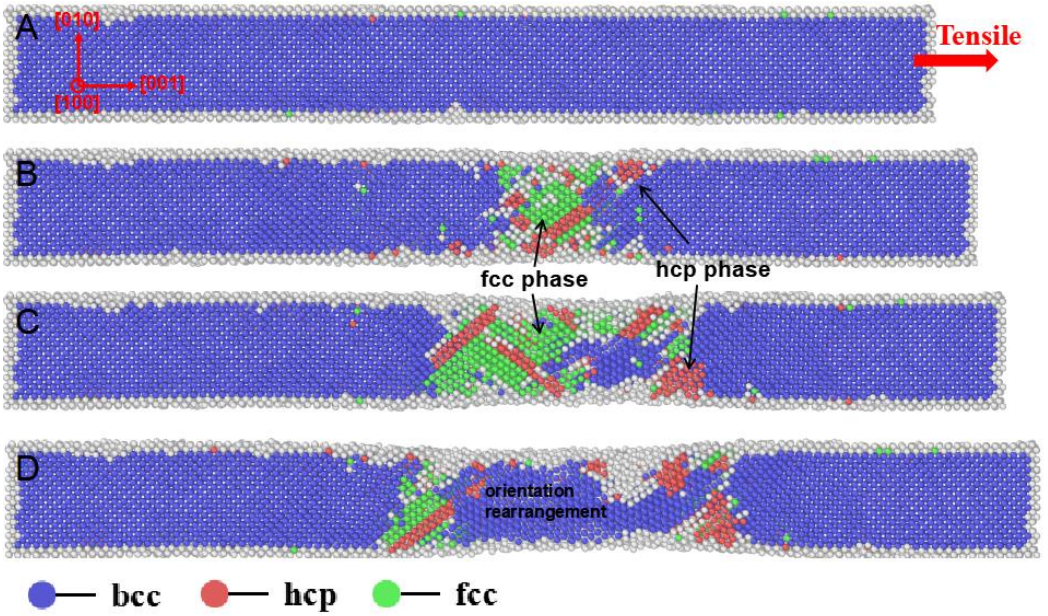

Figure S7. (A-D) illustrates the atomic configuration evolution of a [001]-oriented HfNbTaTiZr HEA NW during tension. One can see that the plastic deformation of this NW is controlled by bcc-fcc phase transition, bcc-hcp phase transition and orientation rearrangement.

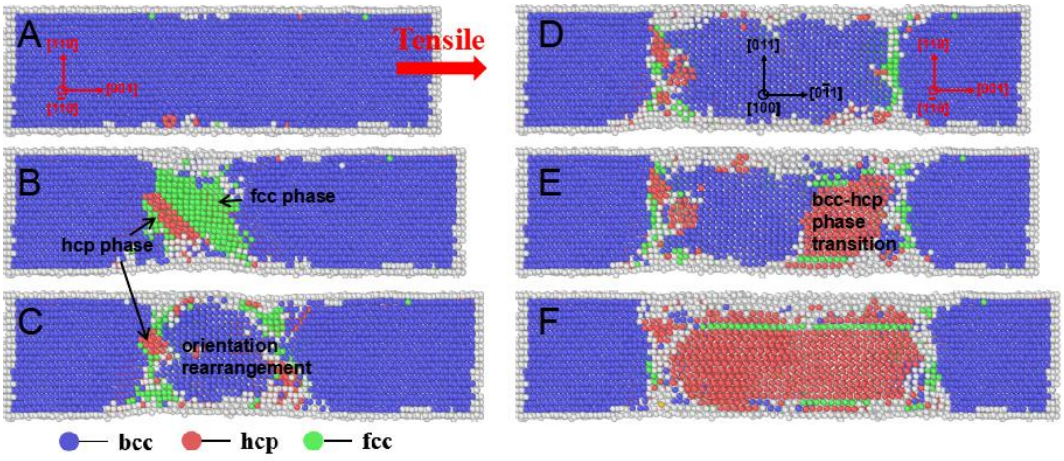

Figure S8. (A-D) illustrates the atomic configuration evolution of another [001]-oriented HfNbTaTiZr HEA NW during tension. One can see that the plastic deformation of this NW is mainly controlled by bcc-fcc phase transition and orientation rearrangement in (A-C). And when the orientation is rearranged to $[0\bar{1}1]$-orientation, the homogeneous bcc-hcp phase transition occurs in (D-F).

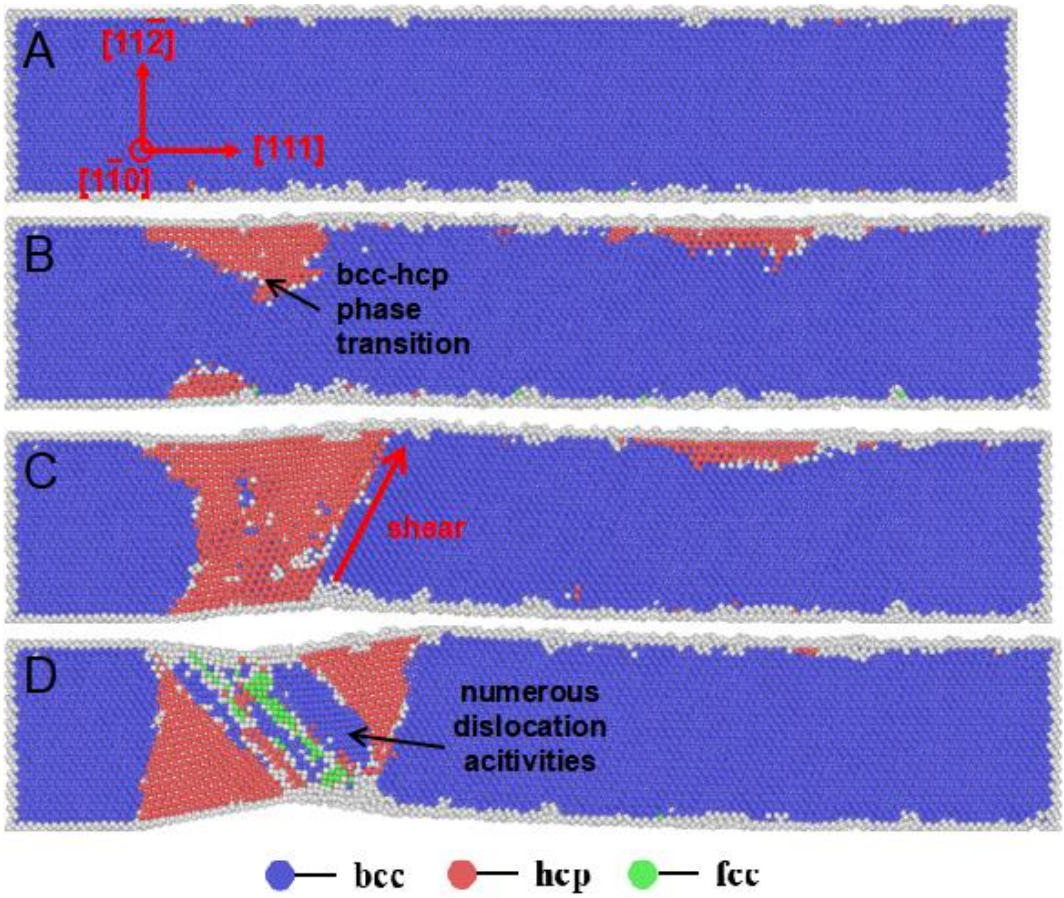

Figure S9. (A-D) illustrates the atomic configuration evolution of a [111]-oriented HfNbTaTiZr HEA NW during tension. Although the bcc-hcp phase transition occurs in (A-C), the NW undergoes significant shear behavior to the extent that this phase transition cannot continue to occur uniformly in subsequent deformations and is eventually replaced by dislocation behavior.

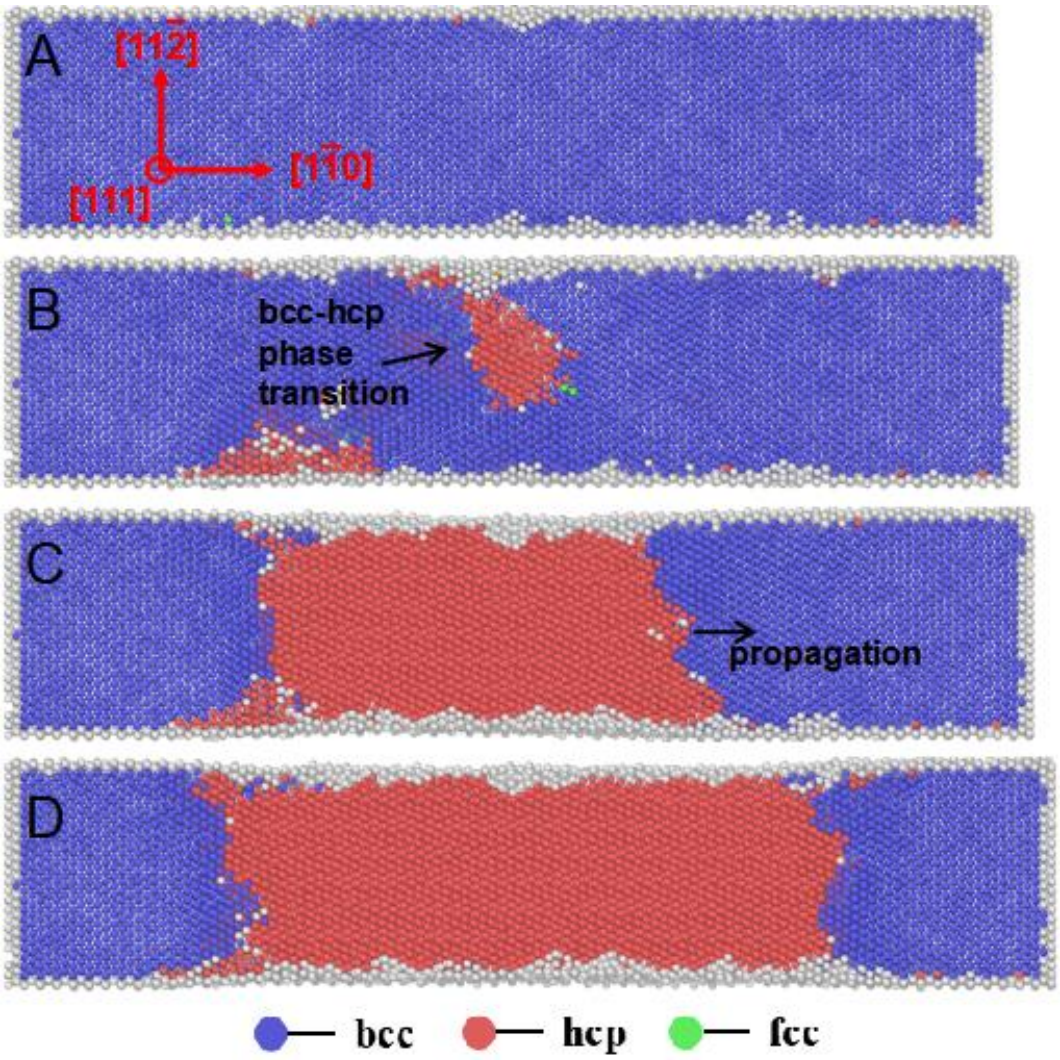

Figure S10. (A-D) illustrates the atomic configuration evolution of another [1$\bar{1}$0]-oriented HfNbTaTiZr HEA NW during tension. The bcc-hcp phase transition occurs and extends continuously and uniformly along the inclined {110} plane.

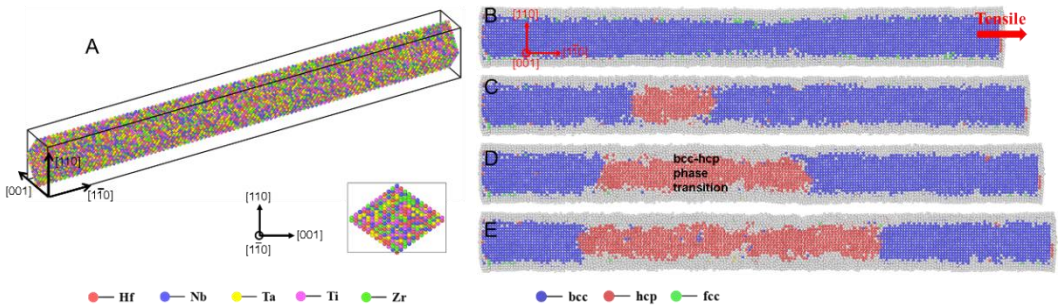

Figure S11. (A) The initial atomic configuration of a [1$\bar{1}$0]-oriented HfNbTaTiZr HEA NW with rhombic cross-section. (B-E) illustrates the atomic configuration evolution of the NW during tension. One can see that the plastic deformation of this NW is mainly controlled by homogeneous bcc-hcp phase transition.

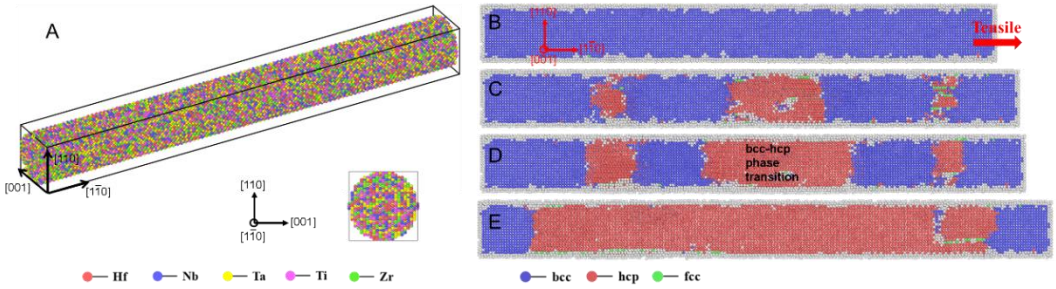

Figure S12. (A) The initial atomic configuration of a [1$\bar{1}$0]-oriented HfNbTaTiZr HEA NW with round cross-section. (B-E) illustrates the atomic configuration evolution of the NW during tension. The bcc-hcp phase transition occurs and extends continuously.

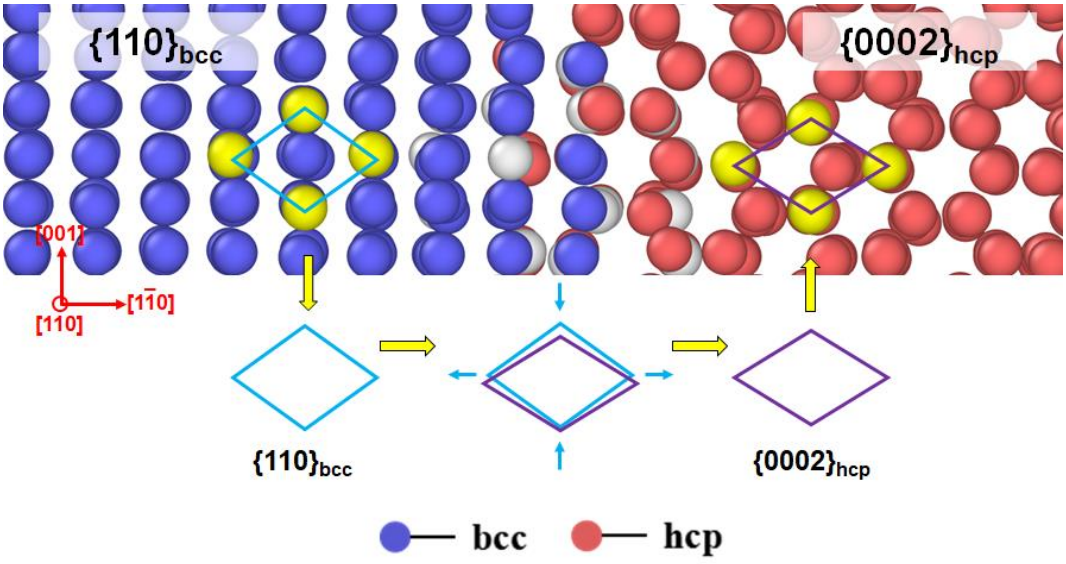

Figure S13. Illustration of the bcc-hcp phase transition of the HEA NW. According to our MD models and previous studies[7], the crystallographic relationship between the bcc structure and the hcp structure before and after the phase transition is $\{110\}_{bcc}$ // $\{0002\}_{hcp}$. Comparing the length parameters of the quadrilateral units (yellow atoms) in the bcc and hcp phases, it show that the bcc lattice transforms into the hcp lattice by elongation along the [1$\bar{1}$0] direction and compression along the [001] direction.

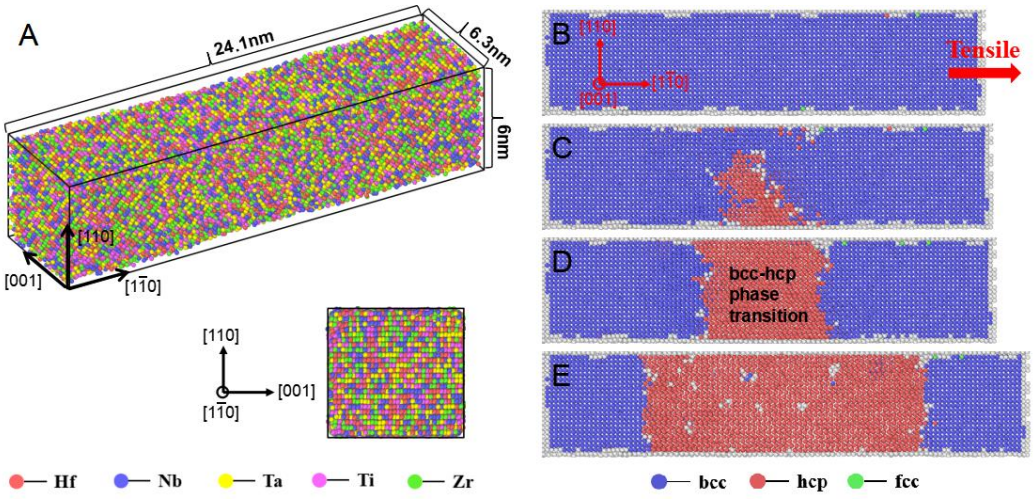

Figure S14. (A) The initial atomic configuration of the HfNbTaTiZr HEA NW with the size of 24.1nm*6.3nm*6nm. (B-E) illustrates the atomic configuration evolution of the NW during tension. One can see that the plastic deformation of this NW is mainly controlled by homogeneous bcc-hcp phase transition.

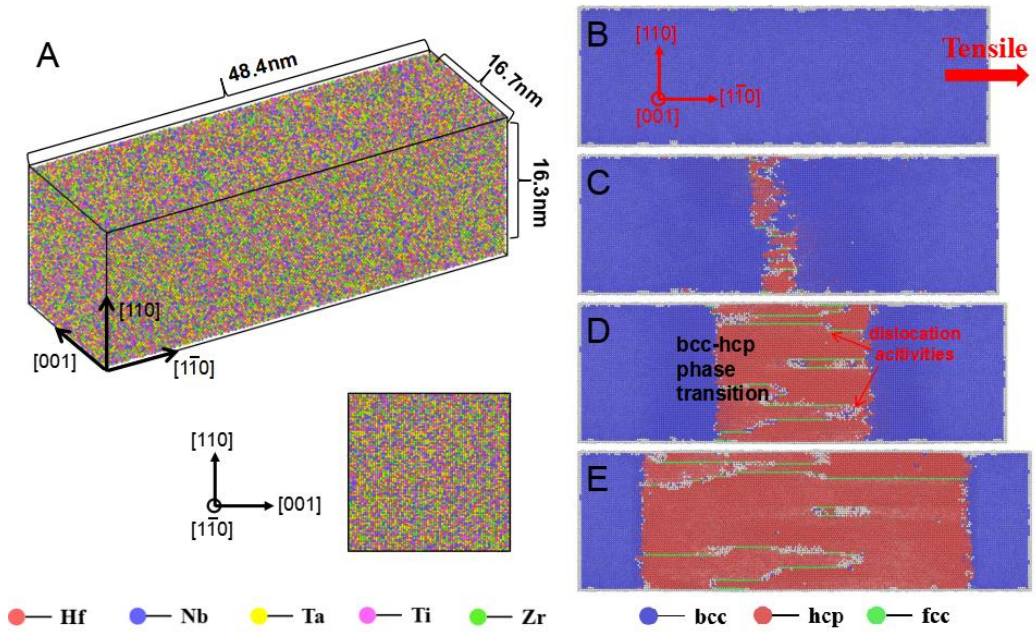

Figure S15. (A) The initial atomic configuration of the HfNbTaTiZr HEA NW with the size of 48.4nm*16.7nm*16.3. (B-E) illustrates the atomic configuration evolution of the NW during tension. One can see that the plastic deformation of this NW is mainly controlled by homogeneous bcc-hcp phase transition, and several dislocations are observed in hcp phase.

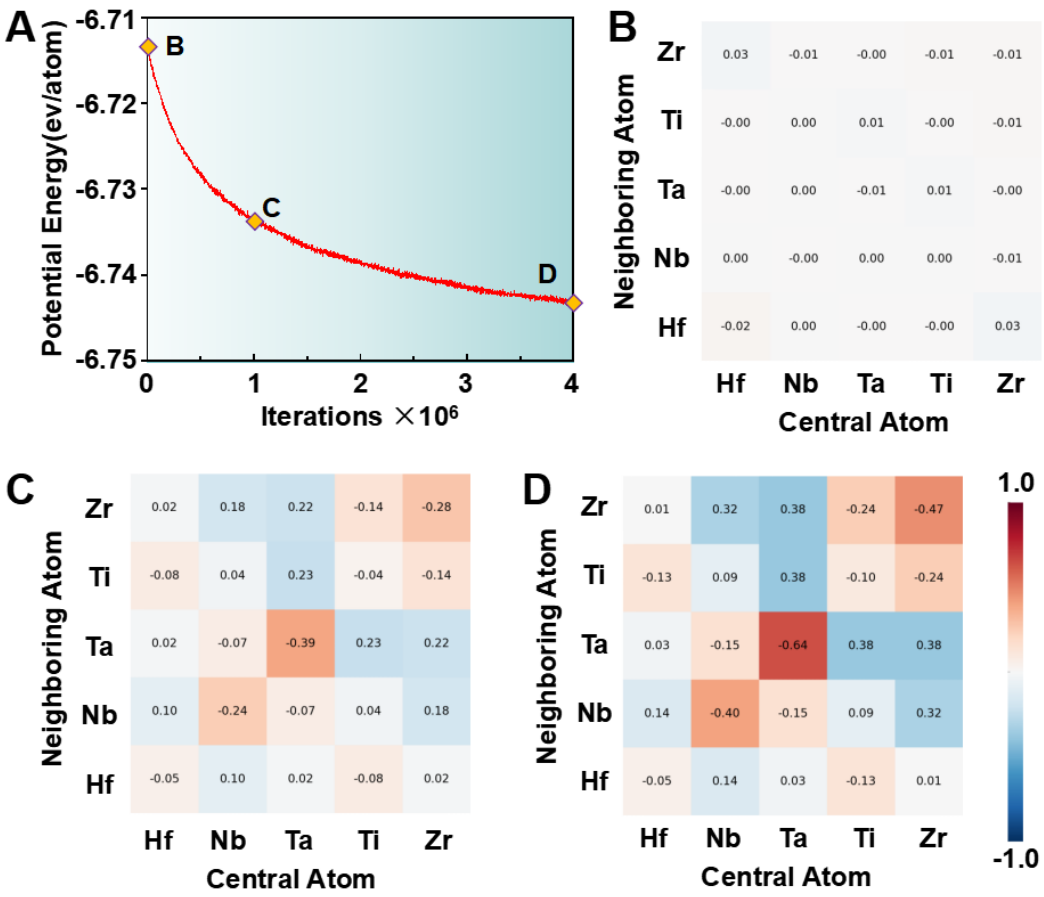

Figure S16. Potential energy and Warren-Cowley parameters of the HfNbTaTiZr HEA during iterations at 300 K. (A) Variation of potential energy with iterations. The potential energy decreases with iterations, suggesting the formation of energetically more favorable atomic configurations. (B-D) Tables of Warren-Cowley parameters at 0 ('B'), 1×10^6 ('C'), and 4×10^6 ('D') iterations, as indicated in (A). Their corresponding atomic constructions are shown in Figures 1, S17 and S18, respectively. It can be seen that the SRO degree of the models increases with iterations.

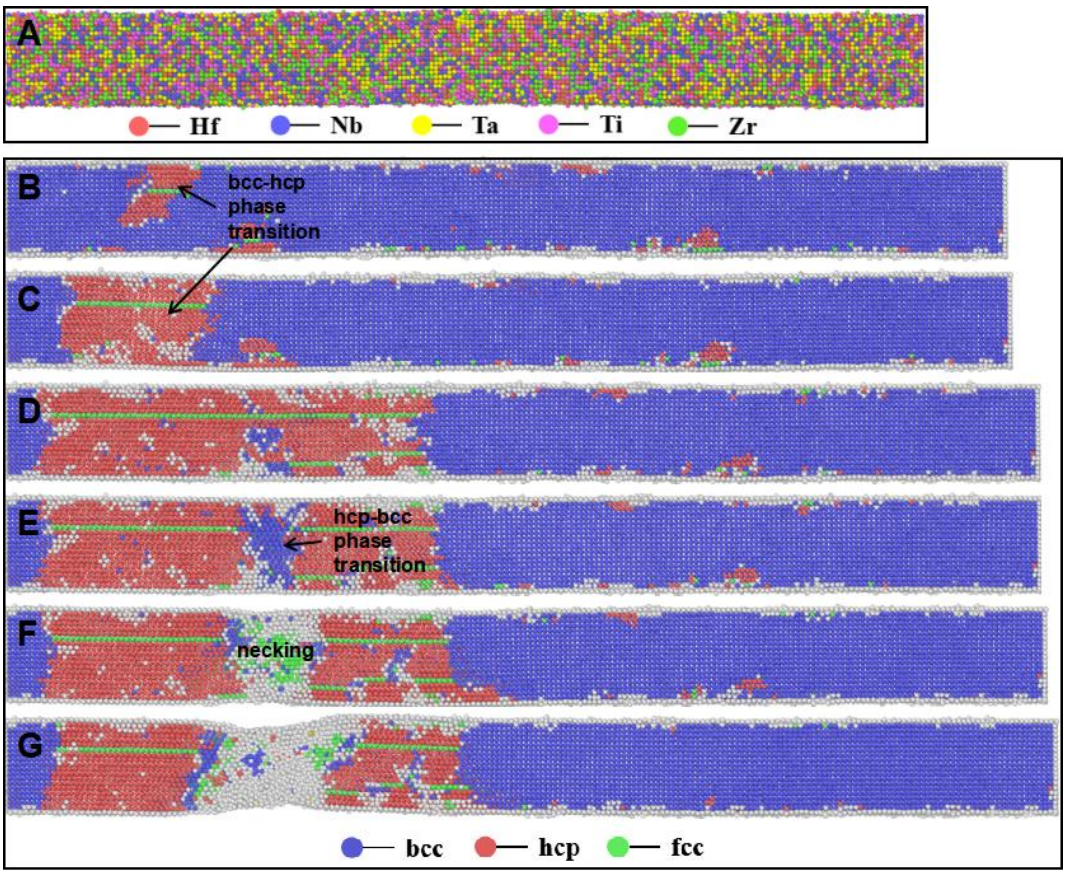

Figure S17. (A) The initial atomic configuration of the $[1\,\bar{1}\,0]$-oriented SRO HfNbTaTiZr HEA NW obtained by 1×10^6 MC iterations. (B-D) The NW undergoes the bcc-hcp phase transition with loading, and the hcp can expand to a considerable size; (E-G) With continues loading, the stress is easily localized due to the presence of the SRO, leading to the NW necking.

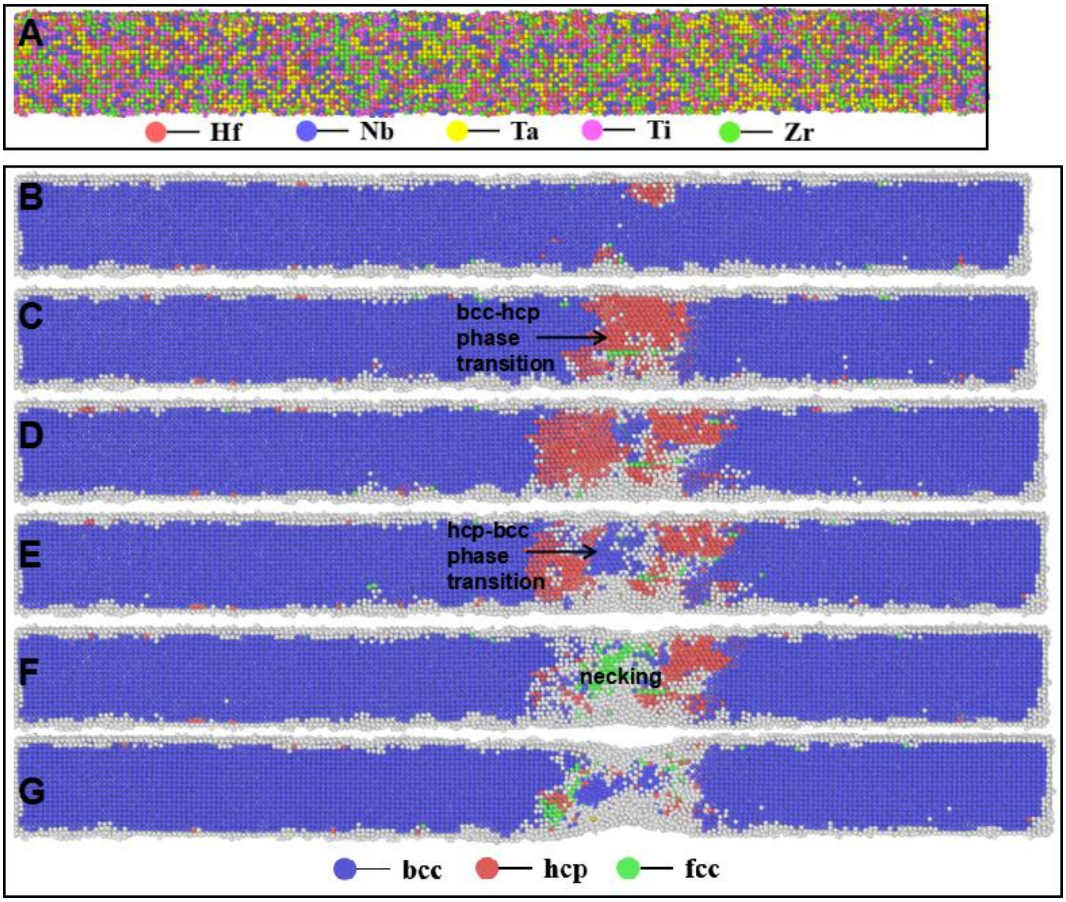

Figure S18. (A) The initial atomic configuration of the $[1\bar{1}0]$-oriented SRO HfNbTaTiZr HEA NW obtained by 4×10^6 MC iterations. (B-D) The plastic deformation of this NW is controlled by the bcc-hcp phase transition. (E) Subsequently, the stress is more easily localized due to the increase in the SRO degree, leading to earlier necking of the NW.

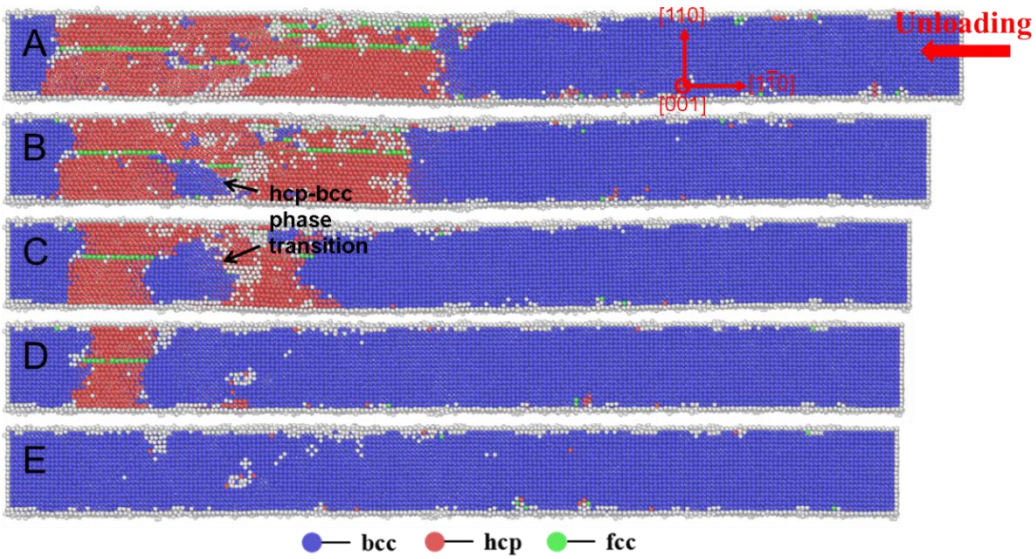

Figure S19. (A-D) illustrates the atomic configuration evolution of the $[1\bar{1}0]$-oriented SRO HfNbTaTiZr HEA NW obtained by 1×10^6 MC iterations during unloading. The reverse bcc-hcp transition occurs not only at the bcc-hcp phase boundary but can also be initiated in the hcp region.

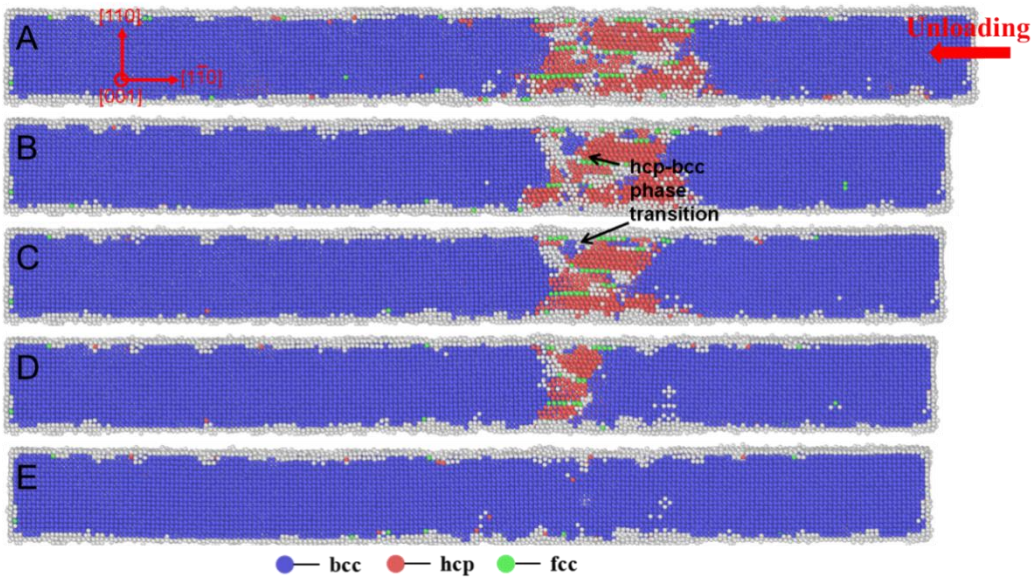

Figure S20. (A-D) illustrates the atomic configuration evolution of the $[1\bar{1}0]$-oriented SRO HfNbTaTiZr HEA NW obtained by 4×10^6 MC iterations during unloading. The reverse bcc-hcp transition occurs not only at the bcc-hcp phase boundary but can also be initiated in the hcp region.

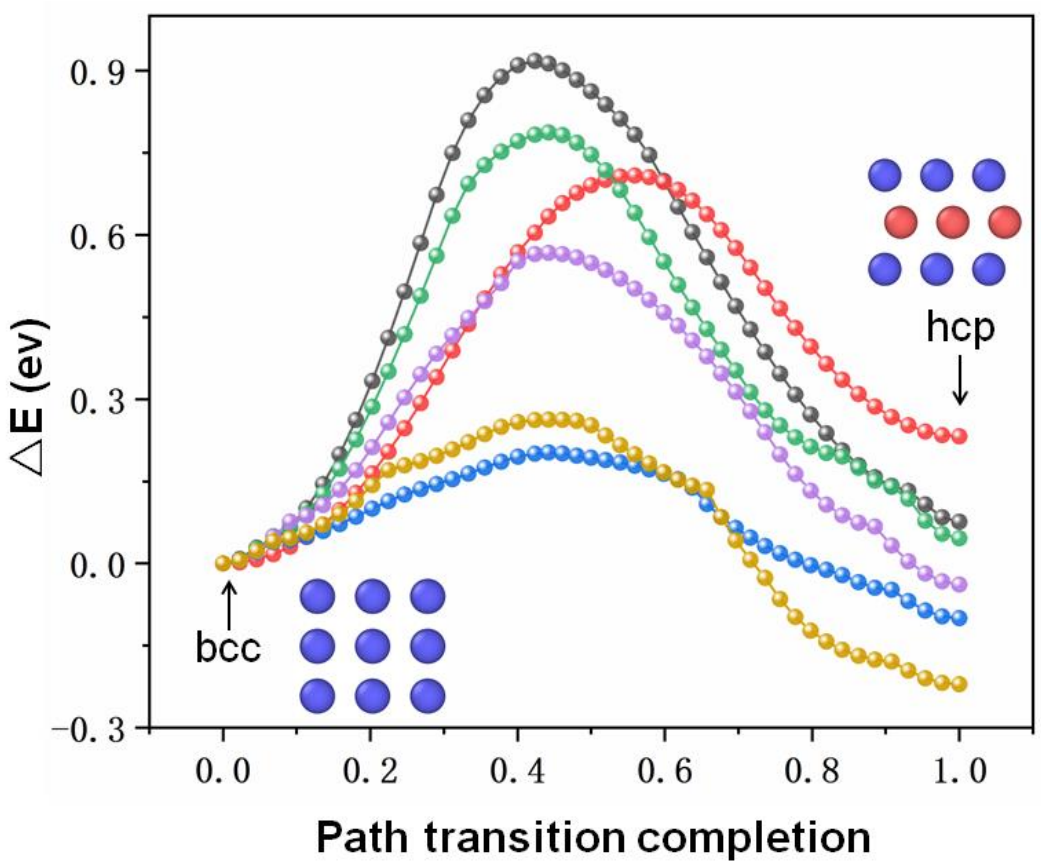

Figure S21. The energy barrier curves associated with the bcc-hcp transition. Curves with different colors correspond to different element distributions. It can be seen that the inhomogeneously distributed elements lead to local variations in the energy barriers for the phase transition.

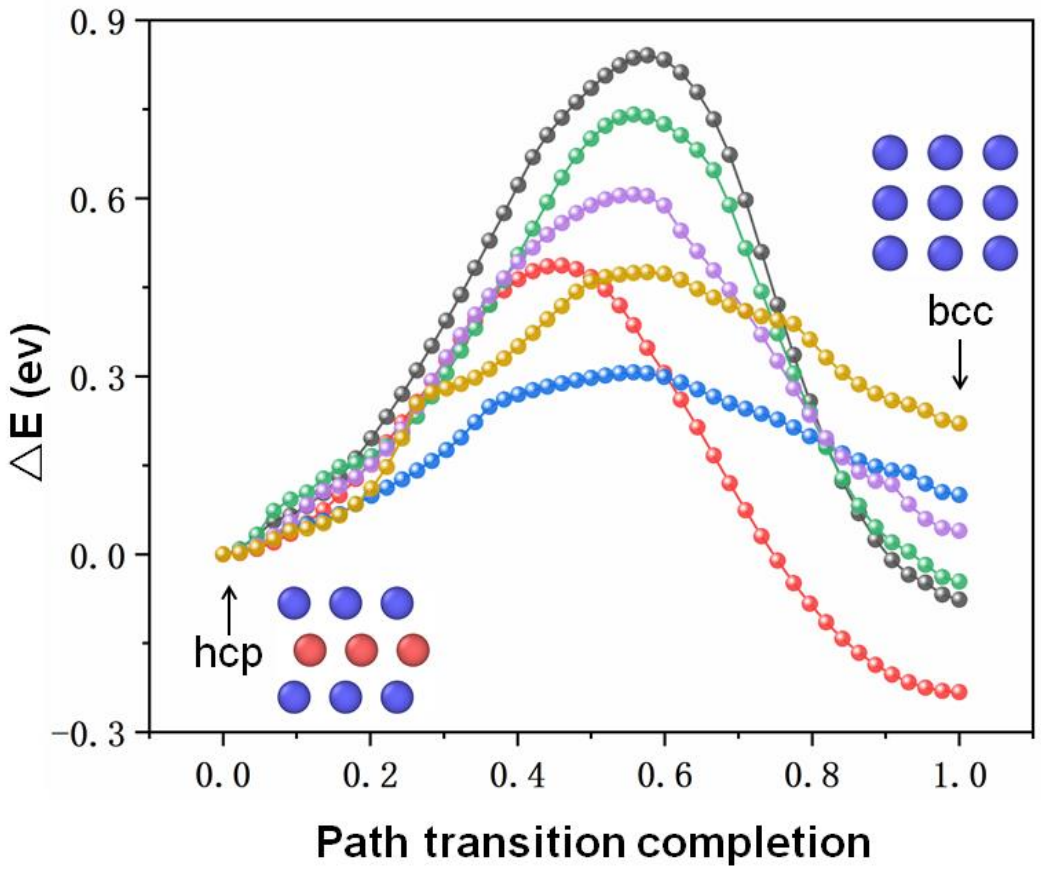

Figure S22. The energy barrier curves associated with the reverse bcc-hcp transition. Curves with different colors correspond to different element distributions. It can be seen that the inhomogeneously distributed elements lead to local variations in the energy barriers for the reverse phase transition.

Reference:

1. Metropolis N, Rosenbluth AW, Rosenbluth MN, et al. Equation of state calculations by fast computing machines. *J Chem Phys* 1953;21:1087–1092. [DOI:10.1063/1.1699114]
2. Nakano A, A space–time-ensemble parallel nudged elastic band algorithm for molecular kinetics simulation. *Comput. Phys. Commun.* 2008;178:280–289. [DOI:10.1016/j.cpc.2007.09.011]
3. Ferrante F, Prestianni A, Bertini M, et al. H2 Transformations on Graphene Supported Palladium Cluster: DFT-MD Simulations and NEB Calculations. *Catalysts* 2020;10:1306. [DOI:10.3390/catal10111306]
4. Buller O, Tewes W, Archer AJ, et al. Nudged elastic band calculation of the binding potential for liquids at interfaces. *J. Chem. Phys.* 2017;147:024701. [DOI:10.1063/1.4990702]
5. Maras E, Trushin O, Stukowski, A, et al. Global transition path search for dislocation formation in Ge on Si (001). *Comput. Phys. Commun* 2016;205:13–21. [DOI:10.1016/j.cpc.2016.04.001]

6. Cowley JM, X-ray measurement of order in single crystals of Cu3Au. *J Appl Phys* 1950;21:24-30. [DOI:10.1063/1.1699415]
7. Larsen PM, Revisiting the common neighbour analysis and the centrosymmetry parameter. *ArXiv 2003* 2020; 08879. [DOI:10.48550/arXiv.2003.08879]
8. Obasi GC, Birosca S, Quinta da Fonseca J, et al. Effect of β grain growth on variant selection and texture memory effect during α→β→α phase transformation in Ti–6Al–4V. *Acta Mater* 2012;60:1048–1058. [DOI: 10.1016/j.actamat.2011.10.038]